MESO-SCALE ANALYSIS OF DUCTILE STEEL FABRIC/EPOXY COMPOSITES: NUMERICAL MODELLING AND EXPERIMENTAL VALIDATION

J. C. Faes*, A. Rezaei, W. Van Paepegem, J. Degrieck

Department of Materials Science and Engineering, Faculty of Engineering and Architecture, Ghent University, Technologiepark-Zwijnaarde 903, B-9052 Zwijnaarde, Belgium
** jana.faes@ugent.be*

Keywords: steel fibers, fabric reinforced composite, meso scale modeling

Abstract
This paper studies the mechanical behavior of steel fiber fabric reinforced epoxy composite on meso scale. The fabric involved is a 4-harness satin weave of innovative steel fibers with a 30 µm diameter. Static tensile tests have been conducted on 4-layer laminates in both principal directions. Mechanical properties were determined based on strain gauge results and full field strain maps were monitored using the Digital Image Correlation technique. Microscopy was performed during the loading process on a polished edge of the coupons. In addition to the experimental study, a finite element unit cell model has been designed based on micro-CT scans of the fabric architecture. An elastic-plastic constitutive behavior was incorporated for both yarns and matrix, in order to fully capture the toughness of this novel material. Both experiments and simulations show that the ductility of the steel fibers could be exploited even more if the cracking of the non-loadbearing yarns could be delayed.

1. Introduction

Improved technologies allow the production of steel fibers with a diameter of about 30 µm, which makes them suitably thin for use as polymer composite reinforcement. A competitive stiffness together with a high ductility that cannot be found among the traditional fiber materials makes these steel fibers very promising for applications in which a high toughness is demanded.

This research focusses on the meso scale mechanical behavior of an epoxy composite with a 4-harness satin weave steel fiber reinforcement. First, results from static tensile experiments on 4-layer fabric laminates are presented. The in-plane mechanical properties were determined based on strain gauge results and damage initiation and evolution were observed microscopically on a polished edge of the coupons during the loading process. The Digital Image Correlation (DIC) technique was employed to map full field surface strains and to detect local strain concentrations. Next, the static tensile behavior of a Representative Volume Element (RVE) of the material structure was analyzed numerically using Abaqus finite element software. Geometry of the RVE was determined using micro-CT scans of the composite material and elastic-plastic constitutive models were proposed for both yarns and matrix.

2. Material

The material under study is a composite of an epoxy matrix and a woven steel fabric reinforcement. The fabric is a 4-harness satin weave (Figure 1.a) with an areal density of 1455 g/m² and a thickness of 0.8 mm. The warp yarns consist of 275 annealed stainless 316L steel fibers with a filament diameter of about 30 µm and the weft yarns are composed of two warp yarns. The fabric was supplied by NV Bekaert SA. The epoxy system is EPIKOTE™ Resin RIM 135 combined with EPIKURE™ Curing Agent RIM H 137. Mechanical properties of the constituent materials can be found in Table 1.

The composite plates with dimensions of 330 x 330 x 3 mm³ (Figure 1.b) were built up using the vacuum assisted resin transfer molding technique (VA-RTM). Resin and hardener were mixed in a 100:30 weight ratio and degassed in a vacuum bell jar, after which the mixture was drawn through a 4-layer stacking of dry fabric under vacuum pressure. The plates were cured at 80°C for 15h according to the manufacturer's recommendations.

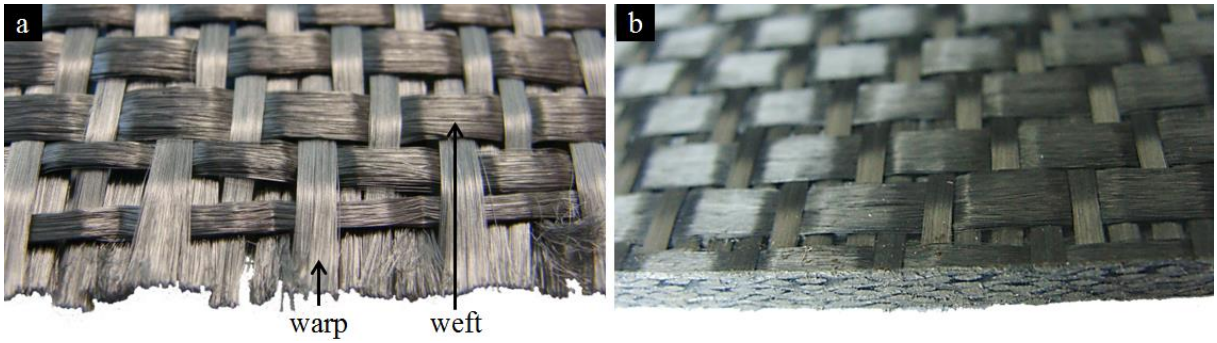

Figure 1. Dry 4-harness satin weave stainless steel fabric (a) and composite steel fabric/epoxy plate (b)

	EPIKOTE™ RIMR 135 epoxy [a]	*Stainless 316L steel fiber* [b]
Mechanical property	**Value**	**Value**
Young's modulus [GPa]	2.73 ± 0.02	193.0
Poisson ratio [-]	0.369 ± 0.013	0.30
Yield strength [MPa]	41.4 ± 2.4	345.0
Ult. tensile strength [MPa]	66.1 ± 0.4	667.0
Failure strain [%]	8.24 ± 0.69	19.5 ± 5.1

[a] Data obtained experimentally by Allaer [1]
[b] Data obtained from NV Bekaert SA

Table 1. Mechanical properties of the constituent materials of the steel fabric/epoxy composites

3. Experiments

3.1. Methodology

Static tensile experiments were carried out in accordance with the ASTM D 3039/D 3039M standard on $[(0F)_2]_S$ and $[(90F)_2]_S$ coupons. Five rectangular test coupons of each type were cut from the composite plates using an abrasive water jet cutter, all with dimensions of 300 x 30 x 3 mm³. No end tabs were used, as preliminary testing had proven them unnecessary. A clamping area with a length of 50 mm was foreseen on both ends of the specimens.

Every coupon was equipped with two strain gauges with a resistance of 350 Ω and a maximum strain of 5 %, in order to measure local strains in the gauge area in both principal directions. On the other side of the specimen, a random speckle pattern was applied for DIC measurements. During the tensile test, this speckle pattern was monitored with a 2 mega-pixel 8-bit CCD AVT Stingray F-201 B1/1.8" camera at a sampling rate of 1 Hz. Afterwards, the MatchID software was used to calculate the displacement fields and the surface strain fields by correlating the consecutive images. Microscopy was performed throughout the loading event on a polished edge of the coupon.

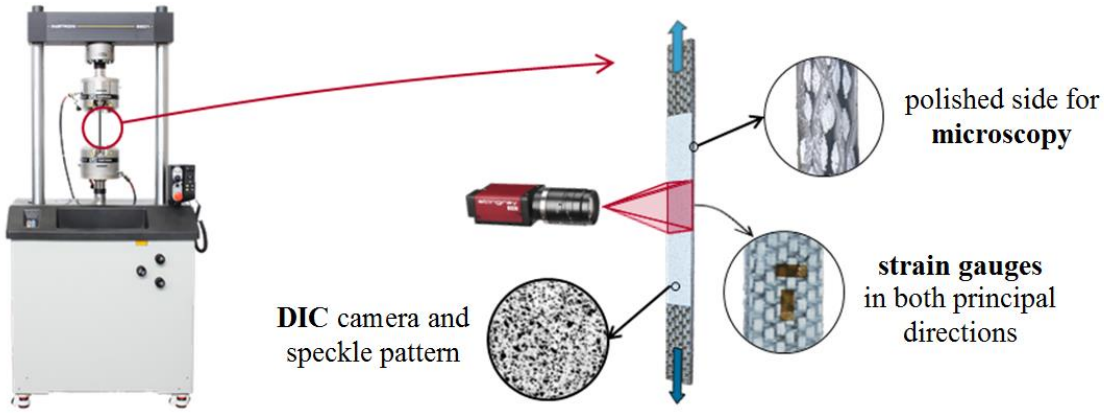

Figure 2. Experimental setup and instrumentation of the steel fabric/epoxy composite tensile specimens

All tensile tests were performed on a servo hydraulic INSTRON 8801 testing machine with a AlignPRO alignment fixture and a load cell of 50 kN. The tests were displacement-controlled with a constant crosshead speed of 2 mm/min. Force and displacement were given by the FastTrack 8800 digital controller with the same time sampling. Strain gauge measurements were acquired synchronously using Labview data acquisition software. DIC results were checked against the strain gauge measurements by extracting the average principal strains over the same area (7 x 3 mm²) and on the same position as the resistance strain gauges.

3.2. Results

The stress-strain response of the $[(0F)_2]_S$ coupons as registrated by the strain gauges and the DIC is shown in Figure 3.a and Figure 3.b, respectively. Analogously, results for the $[(90F)_2]_S$ coupons can be found in Figure 3.c and Figure 3.d. Figure 4 and Figure 5 show the DIC longitudinal strain field (a), the appearance of the failure surface (b), and the damage propagation on the polished side edge of the specimen (c) for both loading directions. The mechanical properties are summarized in Table 2.

The Young's moduli were calculated based on the strain gauge measurements by performing least-squares linear regression fits on the stress-strain curves up to 0.2 % strain. The recommendation in the ASTM to extract the stiffness between 0.1 % and 0.3 % strain was not honored because the stress-strain relation starts to deflect from linearity around 0.2 % strain for this material. Poisson ratios were extracted in the same strain region by making least-square linear regression fits on the transversal strain vs. longitudinal strain curves. The stiffness of the $[(0F)_2]_S$ coupons is approximately 20 % higher than that of the $[(90F)_2]_S$ coupons (E_{11} = 23.9 ± 0.7 GPa versus E_{22} = 19.7 ± 0.5 GPa). Both reciprocal in-plane Poisson ratios, ν_{12} and ν_{21}, were calculated, the former based on the $[(0F)_2]_S$ laminates data and the latter based on the $[(90F)_2]_S$ laminates data. The elastic properties are in reasonable agreement with the orthotropic compliance tensor symmetry condition ($\nu_{12}/E_{11} = \nu_{21}/E_{22}$) [2].

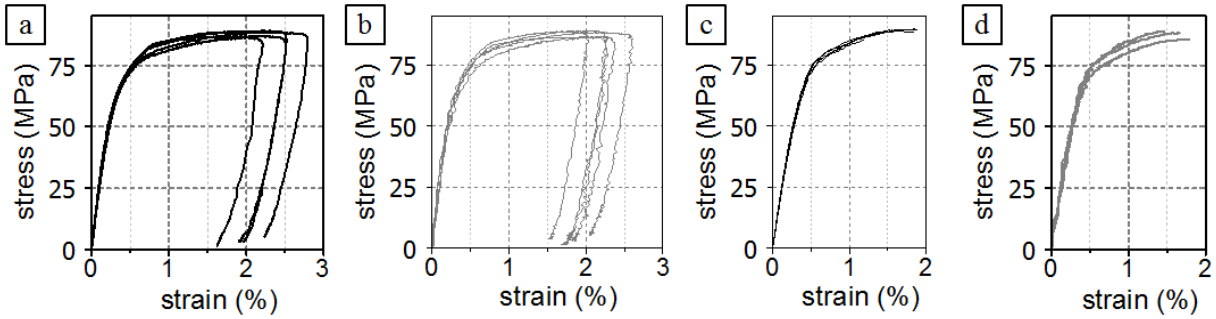

Figure 3. Stress-strain response of the $[(0F)_2]_S$ coupons measured with the strain gauges (a) and with DIC (b) and stress-strain response of the $[(90F)_2]_S$ coupons measured with the strain gauges (c) and with DIC (d)

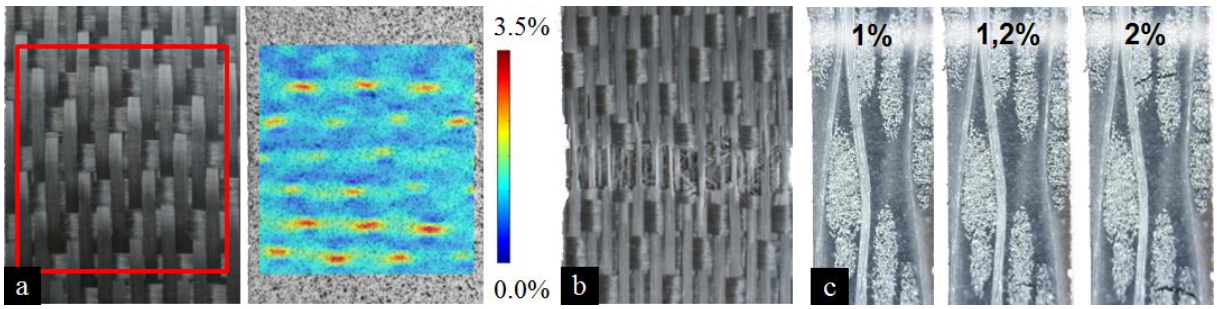

Figure 4. Experimental results for the $[(0F)_2]_S$ steel fabric/epoxy laminates: DIC of the longitudinal surface strain field at 1.2 % global tensile strain (a), appearance of the failure area (b), microscopic images at 1 %, 1.2 % and 2 % global tensile strain, depicting the damage propagation on the polished side edge of the specimen (c)

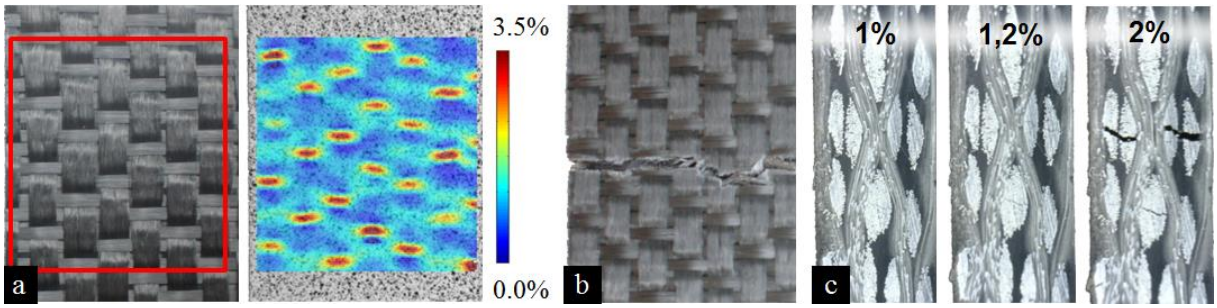

Figure 5. Experimental results for the $[(90F)_2]_S$ steel fabric/epoxy laminates: DIC of the longitudinal surface strain field at 1.2 % global tensile strain (a), appearance of the failure area (b), microscopic images at 1 %, 1.2 % and 2 % global tensile strain, depicting the damage propagation on the polished side edge of the specimen (c)

	$[(0F)_2]_S$ coupons	*$[(90F)_2]_S$ coupons*
Mechanical property	**Value**	**Value**
Young's modulus E_{11} and E_{22} [GPa]	23.9 ± 0.7	19.7 ± 0.5
Poisson ratio ν_{12} and ν_{21} [-]	0.110 ± 0.013	0.086 ± 0.035
Yield strength $\sigma_{Y,0.1\%,11}$ and $\sigma_{Y,0.1\%,22}$ [MPa]	66.5 ± 0.6	69.7 ± 1.4
Yield strain $\varepsilon_{Y,0.1\%,11}$ and $\varepsilon_{Y,0.1\%,22}$ [%]	0.377 ± 0.009	0.456 ± 0.013
Ultimate tensile strength $\sigma_{ult,11}$ and $\sigma_{ult,22}$ [MPa]	87.8 ± 1.1	88.0 ± 1.7
Ultimate tensile strain $\varepsilon_{ult,11}$ and $\varepsilon_{ult,22}$ [%]	2.399 ± 0.281	1.655 ± 0.233

Table 2. Mechanical properties of $[(0F)_2]_S$ and $[(90F)_2]_S$ steel fabric reinforced epoxy laminates

Figure 3 indicates that the composite material's tensile behavior is similar in both principal directions, apart from the final failure mechanism. The 0.1 % offset yield point was recorded

at ($\varepsilon_{Y,0.1\%,11}$ = 0.377 ± 0.009, $\sigma_{Y,0.1\%,11}$ = 66.5 ± 0.6) for the $[(0F)_2]_S$ laminates and at ($\varepsilon_{Y,0.1\%,22}$ = 0.456 ± 0.013, $\sigma_{Y,0.1\%,22}$ = 69.7 ± 1.4) for the [(90F)2]S laminates. After that, the laminates harden until the failure stress is reached. During the hardening process, microscopic cracks appear in the non-loadbearing yarns, all along the gauge length. First evidence of these cracks was observed at about 1.2 % global strain, as can be seen on the microscopic images of the polished edge in Figure 4.c and Figure 5.c. By that time, strain concentrations in the crimp regions up to 3.5% are observed on the DIC analysis results (Figure 4.a and Figure 5.a). The micro cracks continue to grow until the failure stress is reached, which is about 88 MPa, regardless of the loading direction. At this point, the [(90F)2]S laminates fail in a brittle fashion at a strain of 1.655 ± 0.233. The [(0F)2]S laminates, however, stretch up to 2.399 ± 0.281 prior to a slow, continuous raveling of a localized micro crack area, a phenomenon that is responsible for the downwards slope in the stress-strain curves. The difference in appearance of the failure areas accompanying these dissimilar failure modes are visualized in Figure 4.b and Figure 5.b.

3. Numerical analysis

3.1. Representative Volume Element model geometry

The fabric architecture was studied using micro-CT scans of a laminate slice of approximately 25 x 25 x 3 mm³ (Figure 6.a). Micro-CT results were reconstructed and analyzed with Volume Graphics software. Based on these analyses, an RVE was identified (Figure 6.b) and implemented into Abaqus finite element software (Figure 6.c).

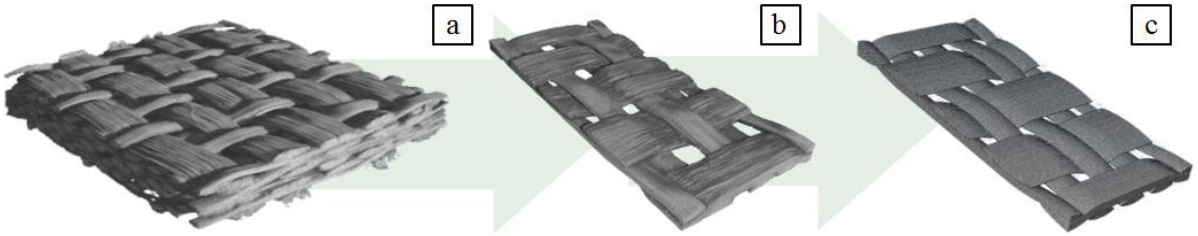

Figure 6. Rendered micro CT-scan images of the full laminate slice (a), the RVE (b) and the corresponding finite element RVE of the fabric (c)

In order to characterize the architecture of the fabric, width and thickness of warp and weft yarns were all measured on every cross-section (Figure 7) and at every yarn crossing. The same strategy was used for determination of the RVE dimensions. The results are summarized in Table 3. In-plane yarn spacing was deduced from RVE dimensions and yarn widths. The through-thickness spacing in between yarns is virtually zero, because four layers of 0.8 mm thick fabric were compacted into a laminate with a thickness of only 3 mm.

a	*warp*	*weft*	**b**	*RVE*
Yarn thickness [mm]	0.38 ± 0.01	0.43 ± 0.01	Warp direction length [mm]	17.26 ± 0.20
Yarn width [mm]	1.51 ± 0.02	3.58 ± 0.17	Weft direction length [mm]	7.74 ± 0.08

Table 3. Yarn dimensions (a) and RVE dimensions (b) from micro-CT scan analysis

A geometrical RVE model was constructed in CATIA® and meshed in Abaqus. A lenticular shape with a 0.02 mm rounding radius was adopted for the yarn profiles, as is overlaid in red on Figure 7.a and Figure 7.b. Cross section areas for warp and weft yarns were calculated as 0.0381 mm² and 0.0440 mm², resulting in fiber volume fractions of 48.7% and 36.4%,

respectively. Yarn tracing was chosen such that the through-thickness inter-yarn distance was kept at a minimum of 5 µm, in view of the finite element meshing feasibility. Yarns were meshed using hexahedral elements, 94717 in total, and the matrix is built of 573169 tetrahedral elements.

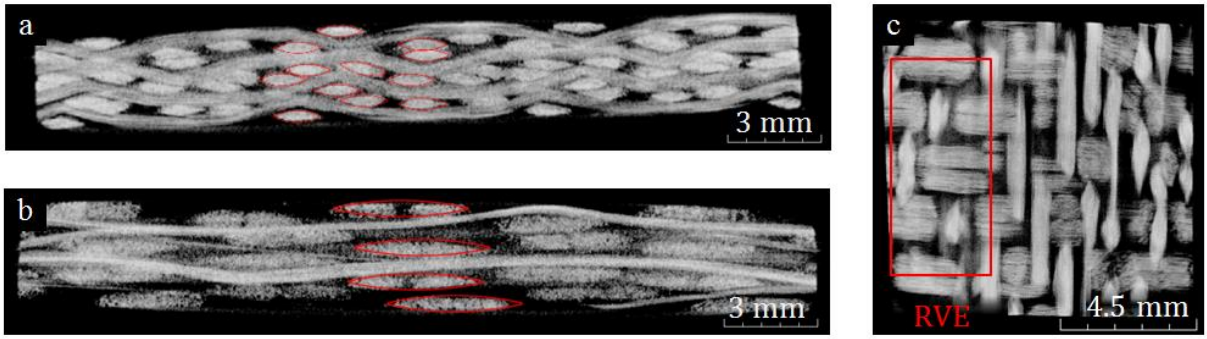

Figure 7. Micro-CT cross-sectional images perpendicular to the warp yarns (a), perpendicular to the weft yarns (b) and perpendicular to the laminate plane (c). Idealized yarn cross sections and RVE are indicated in red.

3.2. Constitutive modeling

The constitutive behavior of the epoxy matrix was modeled using an isotropic plasticity model with a paraboloidal yield criterion and a non-associative flow rule developed by Melro [3]. The elastic constants and hardening functions were fitted on the experimental data of the pure resin by Allaer [1].

Micro-mechanical elastic properties of the transversely isotropic weft and warp yarns were derived from the individual elastic properties of the constituent materials using Chamis [4] analytical homogenization formulas. The results were summarized in Table 4.

	Warp yarns	*Weft yarns*
Mechanical property	**Value**	**Value**
Longitudinal Young's modulus E_L [GPa]	95.457	72.081
Transversal Young's modulus E_T [GPa]	8.759	6.746
Longitudinal Poisson ratio ν_{LT} [-]	0.335	0.344
In-plane Poisson ratio ν_{TT} [-]	0.367	0.368
Longitudinal shear modulus G_{LT} [GPa]	3.204	2.467
In-plane shear modulus G_{TT} [GPa]	3.204	2.467
Initial yield stress σ_{y0} [MPa]	200.0	160.0
Hardening modulus H [GPa]	2.0	2.0

Table 4. Elastic and plastic mechanical properties for the transversely isotropic weft and warp yarns

Tensile testing on unidirectional steel fiber reinforced RIMR 135 epoxy revealed that the elastic regime is followed by a plastic regime with linear hardening when loading in the fiber direction. Transversal loading, on the other hand, causes brittle failure [1]. In order to simulate the plastic deformation of the load-bearing yarns, a plasticity model was introduced with a yield surface Φ being a function of the longitudinal stress σ_{11} and the plastic strain ε^p:

$$\Phi = \sigma_{11} - \left(\sigma_{y0} + H\varepsilon^p\right) \quad (1)$$

Values for the initial yield stress σ_{y0} and the linear hardening modulus H were obtained from the experimental results of the UD material [1] and they can be found in Table 4.

3.2. Numerical analysis and results

The RVE model was subjected to far-field strains in both principal directions using 3D periodic boundary conditions. Figure 8 (a-c) shows the FE results at a strain of 0.24% in the global Z-direction. The loadbearing warp yarns have reached the plastic regime in the crimp regions (Figure 8.a) and the in-plane transverse stress in the weft yarns goes up to 25 MPa (Figure 8.b), which is close to the transverse failure stress of 25.9 MPa that was recorded for the UD laminates [1]. Note that the stress distribution suggests failure initiation on the edges of the weft yarns, opposed to the central cracks that were observed in the experiments. This phenomenon could be attributed to the 3D boundary conditions being too constraining in the Y-direction to simulate the behavior of the 4-layer coupons. Removing the constraints in the Y-direction might cause the stress concentrations to shift towards the yarn centers, as was demonstrated by Daggumati [5]. The matrix is still elastic at this point, with the strain in tensile direction concentrating around the crimp regions. Results of stretching the unit cell up to 1% in the global X-direction are visualized in Figure 8 (d-f). The stresses in the warp yarns reach far beyond the transversal UD failure limit (Figure 8.d), pointing out the urge for implementing an appropriate damage or fracture model for the non-loadbearing yarns. The loadbearing weft yarns are entirely in the plastic regime, as the longitudinal stress exceeds the initial yield stress (Figure 8.e). The plastic deformation in the matrix localizes around the edges of the warp yarns, especially in the crimp regions.

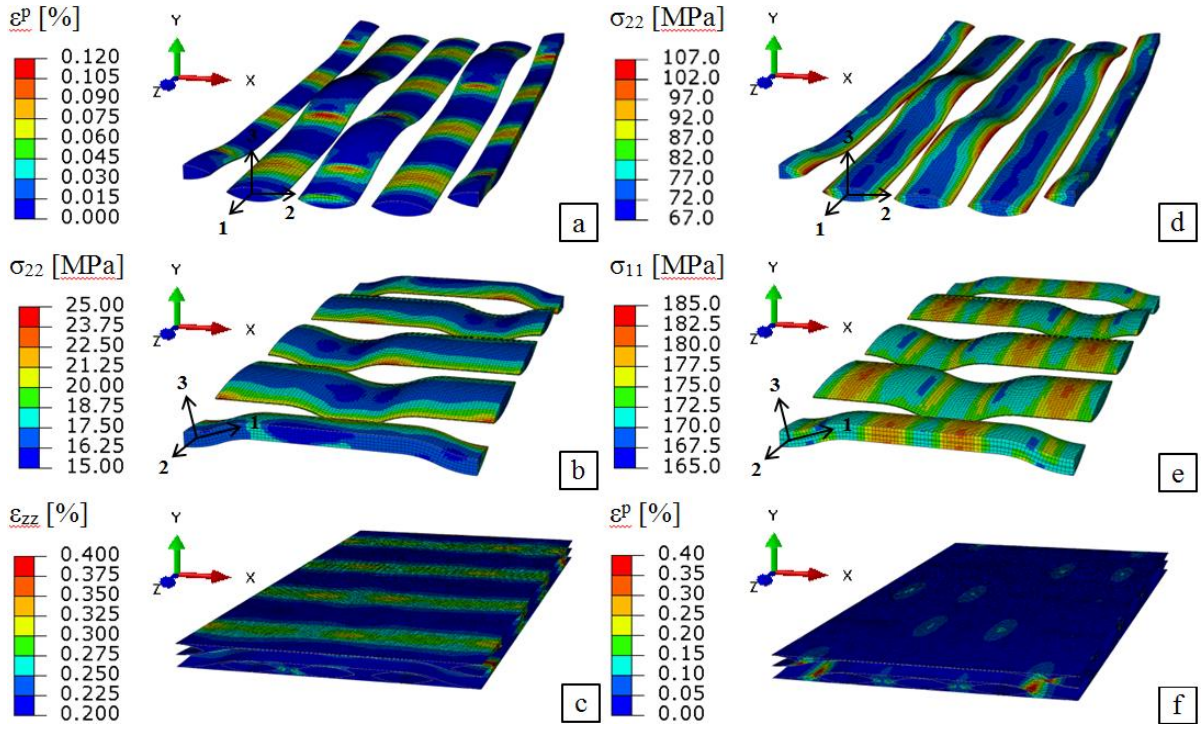

Figure 8. FE analysis results at ε_{zz} = 0.24%: plastic strain in the loadbearing warp yarns (a), transversal stress along the non-loadbearing weft yarns' width direction (b), strain along the tensile direction in the matrix (c), FE analysis results at ε_{xx} = 1%: transversal stress along the non-loadbearing warp yarns' width direction (d), longitudinal stress in the load-bearing weft yarns (e) and plastic strain in the matrix (f)

5. Conclusions

In this paper, the mechanical behavior of steel fiber fabric reinforced epoxy composite was discussed. The involved fabric is a 4-harness satin weave of new steel fibers with a diameter of about 30 µm.

Static tensile tests were carried out in accordance with the ASTM standard on 4-layer laminates. Mechanical properties of the composite were determined based on strain gauge results, and full field strain maps were monitored using DIC technique. Damage initiation and evolution were observed microscopically on a polished edge of the coupons during the loading process. It was found that the composite material behaves similarly in both principal directions, apart from the final failure mechanism. The difference in stiffness between both loading directions was determined to be about 20 %, with values of 23.9 MPa when loading along the warp direction and 19.7 MPa when loading along the weft direction. The elastic regime is followed by a hardening process, and during this process, microscopic cracks appear in the central region of the non-loadbearing yarns. The micro cracks continue to grow until the failure stress is reached, which is about 88 MPa, regardless of the loading direction. At this point, the laminates fail brittly at a strain of 1.655 when tensioned along the weft direction. When loading is applied along the warp direction, however, the laminates stretch up to 2.399 prior to a slow, continuous raveling of a localized micro crack area.

In addition to the experimental study, a finite element RVE model has been developed based on micro-CT scans of the material structure. An elastic-plastic constitutive behavior was incorporated for both yarns and matrix, in order to fully capture the toughness of this novel material. The RVE model was subjected to far-field strains in both principal directions using 3D periodic boundary conditions. The numerical results confirms that damage will initiate in the non-loadbearing yarns, but the stresses in the model concentrate around the yarn's edge, whereas in the experiments, the cracks appeared in the central region of the yarns. Further numerical studies are required to improve the crack initiation prediction.

References

1. K. Allaer, et al., On the In-Plane Mechanical Properties of Ductile Composites Reinforced with Layers of Stainless Steel Fibre, *Manuscript submitted for publication.*, 2014.
2. C.T. Herakovich *Mechanics Of Fibrous Composites*. John Wiley & Son, New York, 1997.
3. A.R. Melro, Analytical and numerical modelling of damage and fracture of advanced composites, *PhD thesis, Faculdade de Engenharia, University of Porto*, 2011.
4. C.C. Chamis, Mechanics of Composite Materials Past, Present and Future, *NASA Contractor Memorandum 100793*, 1984.
5. S. Daggumati, et al., Local strain in a 5-harness satin weave composite under static tension: Part II – Meso-FE analysis. *Composites Science and Technology*, 71(9):1217-1224, 2011.